Title

3D Lead-Organoselenide-Halide Perovskites and their Mixed-Chalcogenide and Mixed-Halide Alloys

Authors

Karunadasa, Hemamala
Li, Jiayi
Wang, Yang
et al.

Publication Date

2024-07-08

DOI

10.1002/ange.202408443

Peer reviewed

RESEARCH ARTICLE

3D Lead-Organoselenide-Halide Perovskites and their Mixed-Chalcogenide and Mixed-Halide Alloys

Jiayi Li,[a] Yang Wang,[b] Santanu Saha,[c] [d] Zhihengyu Chen,[e] Jan Hofmann,[e] Jason Misleh,[a] Karena W. Chapman,[e] Jeffrey A. Reimer,[b] [f] Marina R. Filip,*[c] and Hemamala I. Karunadasa*[a] [g]

[a] J. Li, J. Misleh, Prof. H. I. Karunadasa
Department of Chemistry
Stanford University
Stanford, California 94305, United States
E-mail: hemamala@stanford.edu

[b] Dr. Y. Wang, Prof. J. A. Reimer
Department of Chemical and Biomolecular Engineering, College of Chemistry
UC Berkeley
Berkeley, California 94720, United States

[c] Dr. S. Saha, Prof. M. R. Filip
Department of Physics
University of Oxford
Clarendon Laboratory, Parks Road, Oxford OX1 3PU, United Kingdom
E-mail: marina.filip@ physics.ox.ac.uk

[d] Dr. S. Saha
Institut de Recherche sur les Ceramiques (IRCER), UMR CNRS 7315
Université de Limoges, 12 Rue Atlantis, Limoges 87068, France

[e] Dr. Z. Chen, J. Hofmann, Prof. K. W. Chapman
Department of Chemistry
Stony Brook University
Stony Brook, New York 11794, United States

[f] Prof. J. A. Reimer
Materials Sciences Division
Lawrence Berkeley National Laboratory
Berkeley, California 94720, United States

[g] Prof. H. I. Karunadasa
Stanford Institute for Materials and Energy Sciences (SIMES)
SLAC National Accelerator Laboratory
Menlo Park, California 94025, United States

Supporting information for this article is given via a link at the end of the document.

Abstract: We incorporate Se into the 3D halide perovskite framework using the zwitterionic ligand: SeCYS ($^{+}NH_3(CH_2)_2Se^{-}$), which occupies both the X^{-} and A^{+} sites in the prototypical ABX_3 perovskite. The new organoselenide-halide perovskites: $(SeCYS)PbX_2$ (X = Cl, Br) expand upon the recently discovered organosulfide-halide perovskites. Single-crystal X-ray diffraction and pair distribution function analysis reveal the average structures of the organoselenide-halide perovskites, whereas the local lead coordination environments and their distributions were probed through solid-state ^{77}Se and ^{207}Pb NMR, complemented by theoretical simulations. Density functional theory calculations illustrate that the band structures of $(SeCYS)PbX_2$ largely resemble those of their S analogs, with similar band dispersion patterns, yet with a considerable bandgap decrease. Optical absorbance measurements indeed show bandgaps of 2.07 and 1.86 eV for $(SeCYS)PbX_2$ with X = Cl and Br, respectively. We further demonstrate routes to alloying the halides (Cl, Br) and chalcogenides (S, Se) continuously tuning the bandgap from 1.86 to 2.31 eV—straddling the ideal range for tandem solar cells or visible-light photocatalysis. The comprehensive description of the average and local structures, and how they can fine-tune the bandgap and potential trap states, respectively, establishes the foundation for understanding this new perovskite family, which combines solid-state and organo-main-group chemistry.

Introduction

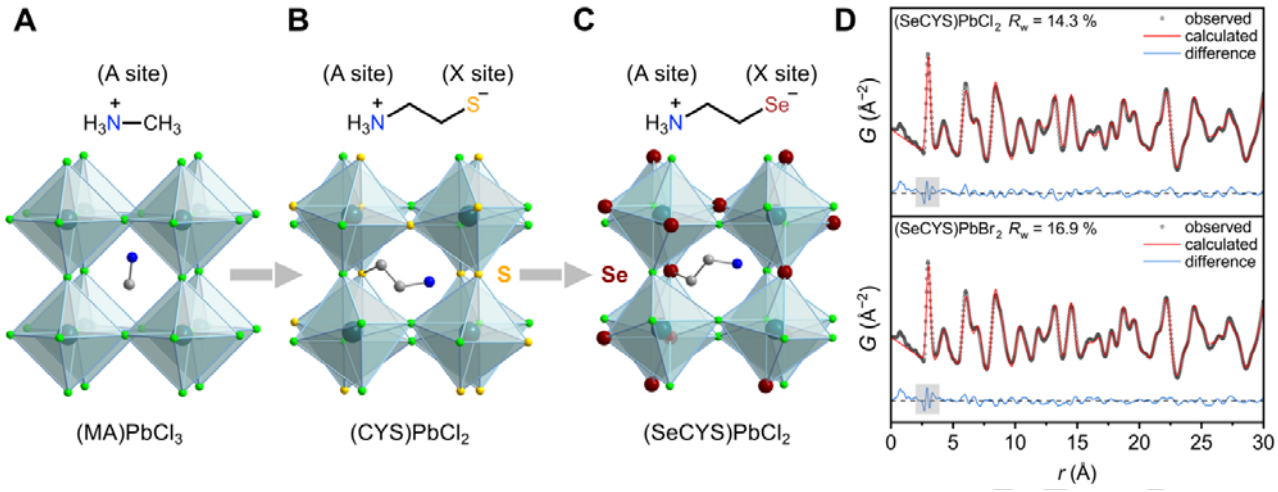

Figure 1. Single-crystal X-ray structures of (A) cubic $(MA)PbCl_3$ (MA = $CH_3NH_3^+$) and of rhombohedral (B) $(CYS)PbCl_2$ (CYS = $^+NH_3(CH_2)_2S^-$) and (C) $(SeCYS)PbCl_2$ (SeCYS = $^+NH_3(CH_2)_2Se^-$). The organic components were unresolved in the structures of (B) and (C) and are shown only as models; disordered atoms are omitted for clarity. The chalcogenide is randomly distributed in the framework, affording different Pb coordination spheres. Turquoise, dark red, green, yellow, blue, and grey spheres represent Pb, Se, Cl, S, N, and C atoms, respectively. H atoms are not shown. (D) Pair distribution function (PDF) fitting of $(SeCYS)PbCl_2$ (top) and $(SeCYS)PbBr_2$ (bottom). The translucent boxes highlight differences between the average structures and the local bond lengths of lead-halide/chalcogenide bonds.

Halide alloying has been widely used to expand the optoelectronic landscape of halide perovskites.[1,2] Indeed, the bandgap and band dispersion of 3D lead-halide perovskites ($APbX_3$; A = monovalent cation, X = halide), which are promising photovoltaic absorbers,[3,4] predictably vary with the electronegativity and size of the halide. Thus, mixing halides in $APbX_3$ perovskites affords bandgaps ranging from 1.5 – 3.0 eV—encompassing near-ideal values for absorbers in single- and multi-junction solar cells.[5–7] However, halide mobility and light-induced halide segregation in mixed-halide compositions have impeded the use of many of these compositions with desirable bandgaps, particularly for multi-junction cells with silicon.[8,9] Thus, other ways of tuning the bandgap of halide perovskites need to be investigated. In order to maintain its exceptional band structure, the halides in the perovskite should ideally be replaced by isolobal, π-donor ligands. We recently reported the new family of 3D organosulfide-halide perovskites: $(CYS)PbX_2$ (CYS = $^+NH_3(CH_2)_2S^-$, X = Cl, Br), where the zwitterionic organosulfide replaces both the A^+ site and an X^- site in the prototypical $APbX_3$ perovskite, introducing sulfide into the perovskite framework.[10] The stronger Pb−S bonds and covalent attachment of the A^+-site cation to the inorganic framework likely contribute to the materials' improved thermal and moisture stability compared to those of $(CH_3NH_3)PbX_3$. DFT calculations show direct bandgaps with dispersive bands in $(CYS)PbX_2$. However, the bandgaps of 2.31 eV and 2.16 eV for the X = Cl and Br analogs, respectively, are still higher than the ideal values (1.7 – 2.0 eV)[11] required for coupling the perovskite with a lower-bandgap bottom absorber in a multi-junction solar cell.

Although the valence band maximum (VBM) of $APbX_3$ perovskites is dominated by halide and Pb states,[12] the VBM of $(CYS)PbX_2$ has mostly S and Pb states, with a markedly smaller halide contribution.[10] Hence, sulfur plays a crucial role in dictating the bandgap magnitudes. The bandgaps of $APbX_3$ decrease monotonically from X = Cl, Br, to I due to the increasing energy of the valence *n*p orbitals in the halide. Therefore, we hypothesized that replacing the S in $(CYS)PbX_2$ with the less electronegative Se may result in a similar bandgap reduction. Indeed, Se alloying in other sulfide-based solar absorbers has reduced the bandgaps, including in chalcopyrite $Cu(In,Ga)(S,Se)_2$ and kesterite $Cu_2ZnSn(S,Se)_4$.[13,14] Selenide perovskites are predicted to exist and are expected to be promising solar absorbers with desirable bandgaps and carrier mobilities.[15–17] However, to our knowledge, there are very few examples of known selenide perovskites ($LaScSe_3$ and uranium-based perovskites)[18] and Se-alloying of oxide perovskites[19,20] requires high-temperature O_2-free synthetic conditions.

Following our strategy of employing zwitterions to introduce chalcogenides into halide perovskites, we describe the synthesis of the first examples of organoselenide-halide perovskites: $(SeCYS)PbX_2$ (Figure 1, X = Cl, Br) using the zwitterion SeCYS ($^+NH_3(CH_2)_2Se^-$). We describe the average and local structures of these materials and show that Se substitution for S indeed reduces the bandgaps (E_g), affording E_g = 2.07 eV and 1.86 eV for X = Cl and Br, respectively, in the ideal range for a multi-junction solar cell with Si. We are further able to alloy the halide (Cl/Br) site or the chalcogenide site (S/Se) to tune the bandgaps continuously from 1.86 to 2.31 eV.

Results and Discussion

Synthesis and Basic Characterization

Replacing CYS with SeCYS, in the synthetic procedure used for $(CYS)PbX_2$, does not afford phase-pure $(SeCYS)PbX_2$ perovskites. Instead, the $(SeCYS)PbX_2$ perovskites required a new synthetic procedure of mixing the lead precursors (ca. 1:1 molar ratio of PbX_2 and $Pb(OAc)_2{\cdot}3H_2O$) and selenocysteamine

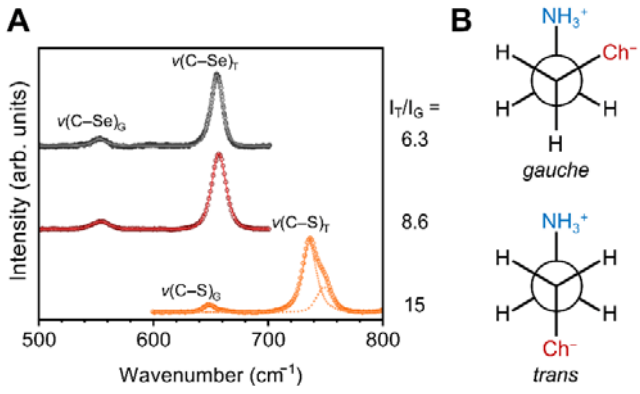

Figure 2. (A) The *trans* and *gauche* *ν*(C–*Ch*) Raman modes (*Ch* = S, Se) in the organochalcogenide-halide perovskites. The I_T/I_G value gives the ratio between *trans* and *gauche* conformers using integrated peak intensities. Open circles: experimental Raman data; solid line: total fit; dashed line: individual fit in $\nu(C–S)_T$ for (CYS)$PbCl_2$. (B) Newman projection of the zwitterionic ligand with two possible rotamers (*trans* and *gauche*).

hydrochloride (SeCYS·HCl) in concentrated NaX aqueous solutions at 90 °C to afford red and black powders for X = Cl and Br, respectively. A lower precursor concentration was used to yield crystals; only the crystals of (SeCYS)$PbCl_2$ were suitable for single-crystal X-ray diffraction (SC-XRD; Figure S1, see the Supporting Information for detailed procedures). We were unable to synthesize the iodide analog using similar synthetic conditions. Elemental analysis of the bulk powder (Combustion analysis for C, H, and N and inductively coupled plasma mass spectrometry for Pb and Se) confirmed the formula as (SeCYS)PbX_2 for both perovskites. X-ray photoelectron spectroscopy (XPS) was also used to estimate the elemental compositions and relative ratios (Figure S3). Solution-state ^{1}H NMR, measured by dissolving the perovskites in deuterated acid, showed that the SeCYS ligand remains unchanged after forming the perovskites.

To probe the ligand environment in the solid (SeCYS)PbX_2, we then applied solid-state ^{13}C NMR with magic angle spinning (MAS). The ^{13}C chemical shifts of the *α*-C and *β*-C are 18.7 ppm (19.0 ppm) and 46.8 ppm (46.9 ppm) for (SeCYS)$PbCl_2$ ((SeCYS)$PbBr_2$), respectively, which are consistent with those in SeCYS·HCl: 17.8 ppm and 44.3 ppm for *α*-C and *β*-C, respectively (Figure S16). The thermogravimetric analyses (scan rate 1 °C/minute) under N_2 atmosphere determine the decomposition temperatures (T_d, corresponding to 5% mass loss) to be 234.5 °C and 222.8 °C for (SeCYS)$PbCl_2$ and (SeCYS)$PbBr_2$, respectively (Figure S5). These values are slightly higher than the values for (CYS)PbX_2 (207.1 °C and 199.0 °C for X = Cl and Br, respectively), presumably due to the less volatile ligand.

The Average Structure of (SeCYS)PbX_2

SC-XRD data of (SeCYS)$PbCl_2$ were solved in the trigonal space group *R*-3*c*, with a disordered organic component ($-CH_2CH_2NH_3^+$) and indistinguishable Se/Cl sites, similar to the SC-XRD solution of (CYS)$PbCl_2$.[10,21] The freely refined occupancies of Cl (0.65) and Se (0.35) in the disordered anion sites are close to the theoretical values (0.67 and 0.33 for Cl and Se, respectively) based on the formula.

The SC-XRD solution reflects the intrinsic disorder of the mixed-anionic perovskite with an organic component that adopts different configurations. For independent structural verification, high-energy X-ray scattering data, suitable for pair distribution function (PDF) analysis, were collected at room temperature using fine powders of (SeCYS)PbX_2. The experimental PDF data were both modeled in the *R*-3*c* space group, only considering the inorganic framework (i.e., Pb and anion sites) in the initial refinement. The anion site was modeled as 1/3 Se and 2/3 X. The contribution of the disordered organic component (~C_2N = 19 electrons) in the cuboctahedral cavity was modeled using a virtual atom with an equivalent number of electrons (K atom) with a large, isotropic atomic displacement parameter reflecting the dynamic disorder of this group. The most significant misfit to experimental data is an asymmetry in the first peak that is associated with the positional Se/X disorder and the resulting distribution of the Pb–Se and Pb–X bond lengths, as seen in other mixed-anion perovskites,[22] which results in local distortions of the Pb-centered octahedra (Figure 1D). The distribution of Pb–Se/X distances was modeled by allowing separate atomic coordinates for the Se and X sites, while constraining the atomic displacement parameters to be isotropic. To best account for local disorder, the PDF data were refined over a short range (2 – 12 Å) (Figure S7). The lattice parameters and fitting results from the long- and short-range PDF refinements are summarized in Tables S2 and S3. The good agreement between the experimental PXRD data and simulated patterns from the PDF models validates the PDF fitting (Figure S2). We then compared the room-temperature cell parameters of the four organochalcogenide-halide perovskites LPbX_2 (L = CYS, SeCYS; X = Cl, Br) all obtained by PDF fitting.[10] A linear lattice expansion is evident from (CYS)$PbCl_2$ < (SeCYS)$PbCl_2$ < (CYS)$PbBr_2$ < (SeCYS)$PbBr_2$ since they crystallize in the same space group and due to the similar radii between Cl^- (1.81 Å) and S^{2-} (1.84 Å) and between Br^- (1.96 Å) and Se^{2-} (1.98 Å) (Figure S8).[23]

Since the inherent disorder of the perovskite crystal structure does not allow us to see the configuration of the organoammonium tail of the organochalcogenide, we obtained Raman spectra of (CYS)$PbCl_2$, (SeCYS)$PbCl_2$, and (SeCYS)$PbBr_2$ to probe the ligand vibrations (Table S7, Figure S4). The Raman spectra were collected at ambient conditions and repeated scans showed no signs of material decomposition, by oxidation or laser damage, over 10 minutes. The low-energy Raman signals below 200 cm^{-1} are assigned to lattice phonon modes through comparison to the Raman data of (MA)PbX_3 perovskites.[24,25] We observed a redshift of lattice modes with S to Se and Cl to Br substitution. The higher-energy modes (>200 cm^{-1}) are attributed to CYS/SeCYS ligand modes, which we assigned based on reported experimental/theoretical studies on CYS (see Table S7 for assignments). The peaks at 380 and 327 cm^{-1} in the spectra of (CYS)$PbCl_2$ and (SeCYS)$PbCl_2$, respectively, are assigned to the C–N torsion mode. In (MA)PbX_3 perovskites, this mode is more pronounced and broader due to the free rotation of MA^+. For (CYS)PbX_2 and (SeCYS)PbX_2, the C–N rotation is more restricted due to sterics and covalent

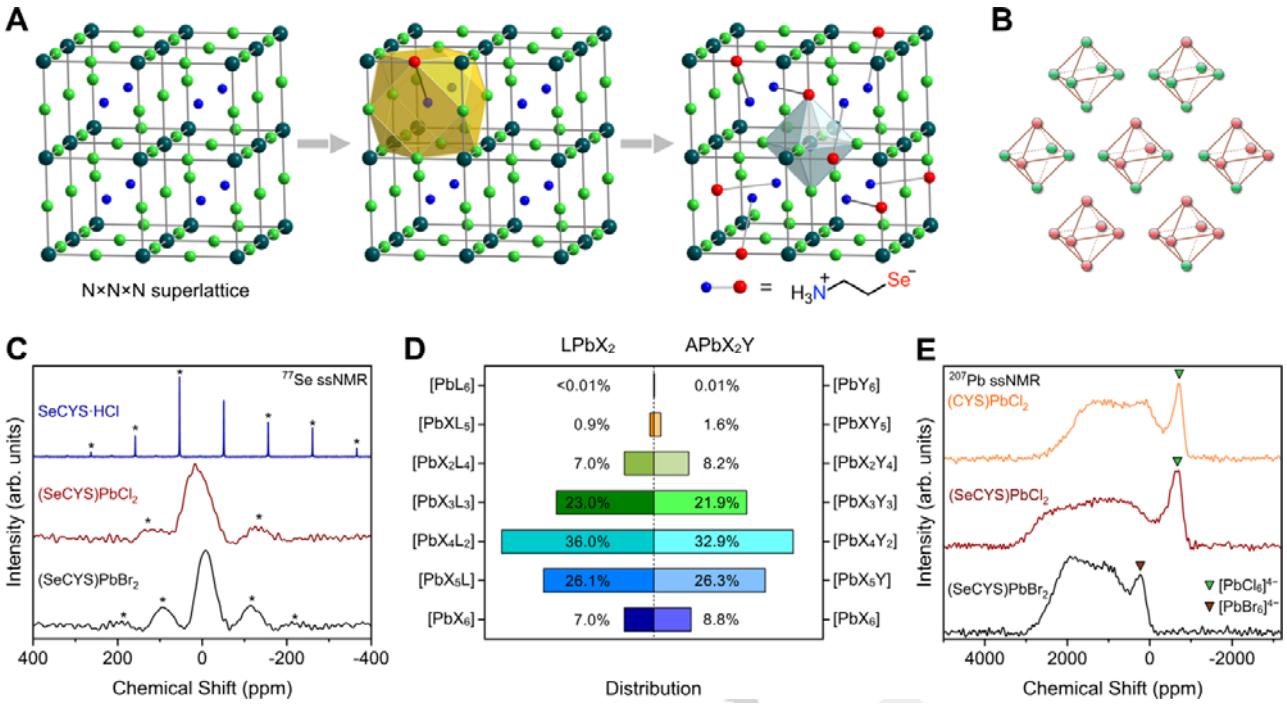

Figure 3. (A) Stepwise illustration of the algorithm used to simulate the random distribution of the organochalcogenide ligand in $LPbX_2$ (L = CYS, SeCYS, X = Cl, Br). Step 1: Construct a 200 × 200 × 200 superlattice of the prototypical perovskite $APbX_3$. Dark turquoise, light green, blue spheres represent Pb, halide, and A^+-site cations, respectively. Step 2: For each A^+ site, find the closest 12 halides (shown in the yellow truncated cube) and randomly choose one to be chalcogenide (red sphere). The connection between the A^+ site and the chalcogenide stands for a zwitterionic organochalcogenide ligand. Step 3: After repeating step B for all A^+ sites, find the coordination environments for the Pb centers (shown in the light blue octahedron). (B) The seven distinct coordination environments of Pb octahedra (not distinguishing between *cis/trans* isomers). The green and red spheres represent the halide and ligand (L = SeCYS, CYS), respectively. (C) ^{77}Se ssNMR spectra of SeCYS·HCl, $(SeCYS)PbCl_2$, and $(SeCYS)PbBr_2$ with a magic-angle spinning (MAS) frequency of 10 kHz at 11.7 T. The asterisks (*) indicate spinning sidebands (identified by varying MAS frequencies, see Figure S16). (D) Comparison of distributions of different Pb coordination spheres, between the fully disordered $LPbX_2$ perovskite (left) and the mixed-halide $APbX_2Y$ perovskite (right) (A = monocation, L = zwitterion, X and Y are different halides). (E) ^{207}Pb ssNMR spectra (without spinning) of $(CYS)PbCl_2$, $(SeCYS)PbCl_2$, and $(SeCYS)PbBr_2$, acquired at 11.7 T. The triangles indicate the peaks assigned to $[PbX_6]^{4-}$.

bonding between Pb and S/Se, resulting in a peak with much weaker intensity. Next, we analyzed the highly polarizable C–*Ch* (*Ch* = S, Se) stretching vibrations. Importantly, these modes are well-known to be sensitive to the rotational isomerization around the C–C bond.[26–30] In $(CYS)PbCl_2$, the peaks for the *gauche* (G) and *trans* (T) C–S stretching modes are centered at 650 and 738 cm^{-1}, respectively. This is consistent with the reported values of 640 and 725 cm^{-1}, observed for CYS chemisorbed on a Ag surface via the terminal S.[31] We observe two closely spaced $\nu(C–S)_T$ modes in $(CYS)PbCl_2$ (at 736, 749 cm^{-1} by fitting), possibly from two *trans* conformers with slightly different rotational angles. In $(SeCYS)PbX_2$, the $\nu(C–Se)_G$ and $\nu(C–Se)_T$ peaks center at 550 (554) and 654 (655) cm^{-1}, respectively, for X = Cl (Br). The relative ratios of the two conformers can be semi-quantitatively calculated from the integrated peak intensity ratios (I_T/I_G) for $\nu(C–Ch)_T$ and $\nu(C–Ch)_G$. At ambient conditions, the zwitterionic ligands prefer to adopt a *trans* conformer inside the cuboctahedral cavity of the perovskite, with I_T/I_G = 15, 8.6, and 6.3 for $(CYS)PbCl_2$, $(SeCYS)PbCl_2$, and $(SeCYS)PbBr_2$, respectively. The most intense peak (ca. 1230–1260 cm^{-1}) is tentatively assigned to the twisting/wagging modes of the methylene groups, which have also been observed as strong peaks (ca. 1220–1230 cm^{-1}) in the Raman spectrum of $(Az)PbX_3$ (Az = aziridinium), although assigned differently.[32]

The Local Structures in $LPbX_2$ (L = CYS and SeCYS).

Since the organochalcogenide-halide perovskites are heteroanionic materials[33,34] with anion disorder, a closer look at their local structures is warranted. Previous structural studies of $(CYS)PbX_2$ through X-ray scattering (SC-XRD, PXRD, PDF) indicated disordered sulfide and halide sites in the long-range or average structure.[10] Yet, the local ordering of anions around the Pb center remains unknown. We first applied solid-state ^{77}Se NMR to probe the chemical environment of the selenide in the solid. The Pb−Se bonding dramatically changes the ^{77}Se chemical shift from −51.3 ppm (free ligand) to 4.7 ppm and −6.0 ppm for $(SeCYS)PbCl_2$ and $(SeCYS)PbBr_2$, respectively, indicating the formation of metal-selenide bonds.[35,36] The broad linewidths of the ^{77}Se signals in the perovskites are attributed to the local disorder in the structure (Figure 3C).

Solid-state ^{207}Pb NMR has served as a powerful tool to directly probe the local environment of Pb and investigate halide order on the local scale in lead-halide perovskites.[37,38] The ^{207}Pb nuclide, with I = 1/2, at 22% abundance, and with high receptivity (12 times compared with that of ^{13}C), enables the NMR measurements to be relatively accessible.[39] The chemical shift, spanning a large window (~20,000 ppm) and linewidth are both

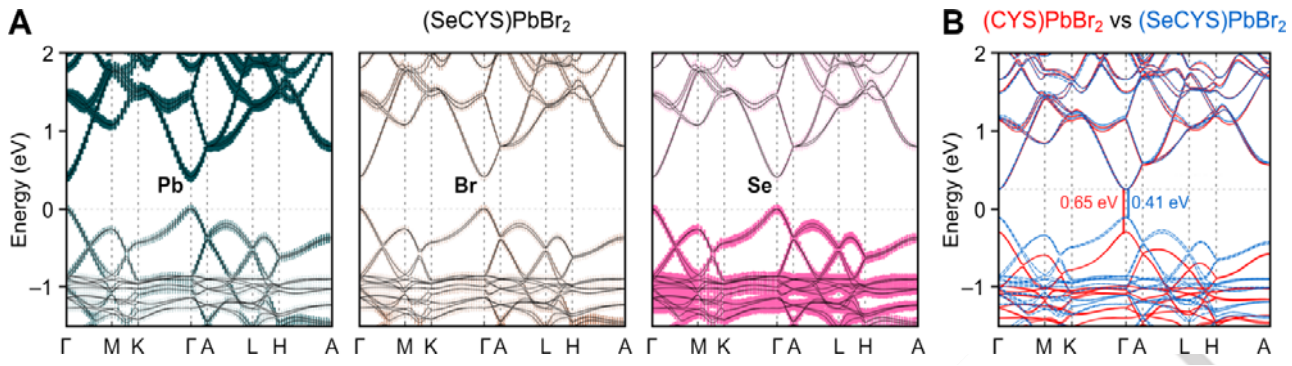

Figure 4. (A) Band structures of (SeCYS)$PbBr_2$. The Pb, Br, and Se orbitals that contribute to the bands are depicted as turquoise, brown, and magenta dots, respectively, where the dot size is proportional to the atomic contribution. The band structure is calculated along the high symmetry path Γ (0,0,0) − M (0.5,0,0) − K (0.333,0.333,0) − Γ (0,0,0) − A (0,0,0.5) − L (0.5,0,0.5) − H (0.333,0.333,0.5) − A (0,0,0.5).[47] The SeCYS molecules are modeled as ordered (see Supporting Information). (B) Comparison of the band structures of (CYS)$PbBr_2$ and (SeCYS)$PbBr_2$, where the conduction band minima have been arbitrarily aligned.

highly sensitive to the local coordination.[40] The coordination environments of Pb in mixed-Cl/Br 3D perovskites have been identified by ^{207}Pb NMR to be $[PbCl_6]^{4-}$, $[PbCl_5Br]^{4-}$, $[PbCl_4Br_2]^{4-}$, $[PbCl_3Br_3]^{4-}$, $[PbCl_2Br_4]^{4-}$, $[PbClBr_5]^{4-}$, and $[PbBr_6]^{4-}$.[40–42] The ratios of these seven environments are consistent with the binomial distribution (Figure 3D), which indicates that the two anions randomly occupy the X^- site to form solid solutions.

Here, we considered the two extreme local orderings of Pb coordination in the $LPbX_2$: (1) fully ordered: each Pb is coordinated by two chalcogenides and four halides; (2) fully disordered: the chalcogenide ligands randomly distribute in the framework. In the first scenario, we would expect only one chemical environment of Pb, corresponding to one ^{207}Pb NMR signal arising from $[PbL_2X_4]^{2-}$ (not distinguishing between *cis*/*trans* isomers). For the fully disordered distribution, there are 7 possible local structures, $[PbL_{6-x}X_x]^n$ (x = 0, 1, 2, …, 6), which closely resembles the case of mixed-halide perovskites (Figure 3B). The theoretical distributions of L and X in the $LPbX_2$ perovskites are more complicated than the simple binomial distribution observed in mixed-halide perovskites due to the additional restraint that the zwitterions must connect the A^+ site and anion site. We designed an algorithm to simulate the distribution of Pb coordination environments in $LPbX_2$ using a large superlattice (200 × 200 × 200) assuming fully disordered ligands (Figure 3A, see Supporting Information for assumptions and code). The calculation results are similar, though not identical, to the theoretical distribution of Pb coordination spheres in mixed-halide perovskites with a halide alloying ratio of 1:2, as shown in Figure 3D.

We obtained the solid-state ^{207}Pb NMR spectra of (CYS)$PbCl_2$, (SeCYS)$PbCl_2$, and (SeCYS)$PbBr_2$ as shown in Figure 3E. All three materials exhibit a wide range of ^{207}Pb signals, from −1000 ppm to 3000 ppm, with a relatively narrow peak at a lower frequency followed by a broad main peak at a higher frequency. The wide NMR spectra were collected using the variable offset cumulative spectra (VOCS) approach.[43] The resulting spectra are full chemical shift powder patterns, yet we can assign the features according to the local bonding environment. The narrow peaks at the lower frequency are assigned as the $[PbX_6]^{4-}$ species ($[PbCl_6]^{4-}$: −696 ppm and −656 ppm in (CYS)$PbCl_2$ and (SeCYS)$PbCl_2$, respectively, and −646 ppm in (MA)$PbCl_3$; $[PbBr_6]^{4-}$: 232 ppm in (SeCYS)$PbBr_2$, 344 ppm in (MA)$PbBr_3$). The differences in the ^{207}Pb NMR chemical shift observed in different perovskites even for the same local coordination (e.g., for $[PbCl_6]^{4-}$ in (CYS)$PbCl_2$ and (SeCYS)$PbCl_2$) show the sensitivity of the NMR signal to the next-next-nearest neighbors, as seen in the NMR spectra of (MA)$PbX_{3-x}Y_x$ (X, Y = halides) as well.[42] The broad signals are therefore attributed to chalcogenide-containing species $[PbL_{6-x}X_x]^n$ (L = CYS, SeCYS; x = 1, 2, 3, …, 6). The existence of $[PbX_6]^{4-}$ species rules out the fully ordered structure. We then integrated the $[PbX_6]^{4-}$ peaks to obtain their ratios in the whole spectra semi-quantitatively. The ratios of $[PbX_6]^{4-}$ were estimated to be 11%, 16%, and 11% in (CYS)$PbCl_2$, (SeCYS)$PbCl_2$, and (SeCYS)$PbBr_2$, respectively, which are consistent, within the precision of the measurement, with the theoretical ratio of $[PbX_6]^{4-}$ calculated for the fully disordered model (7.0%).

Two-dimensional ^{207}Pb exchange spectroscopy (EXSY) spectra were also collected at room temperature with a mixing time of 2 ms (Figure S17). Due to the wide range of ^{207}Pb signals, we were unable to measure 2D EXSY covering the whole range

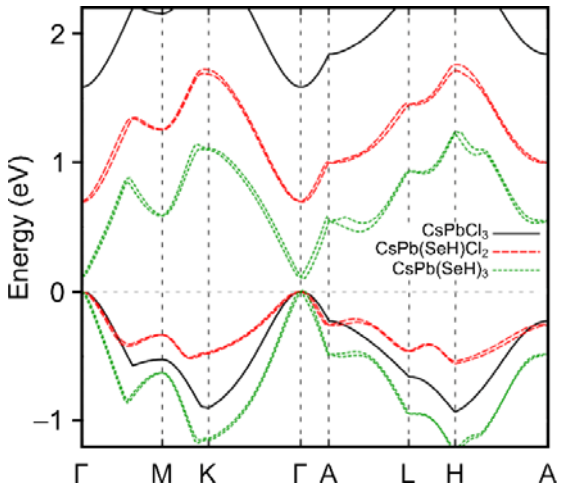

Figure 5. Comparison of the band structures of hypothetical $CsPbCl_3$, *trans*-$CsPb(SeH)Cl_2$, and $CsPb(SeH)_3$ all in the *R*-3*c* space group. The valence-band maxima have been arbitrarily aligned, for ease of comparison.

within a feasible timescale. Therefore, we selectively excited at −720 ppm and 240 ppm for (CYS)$PbCl_2$ and (SeCYS)$PbBr_2$, respectively, to obtain signals from $[PbX_6]^{4-}$ and from some $[PbL_{6-x}X_x]^n$ species. In contrast to the mixed-halide perovskites, where halide exchange causes cross-peaks in room-temperature 2D EXSY,[40] no cross-peaks were observed, indicating the absence of halide/chalcogenide ligand exchange in the $LPbX_2$ perovskites. The immobility of the organochalcogenide can be explained by the stronger bonding interaction between Pb and the chalcogenide and the expected low mobility of the larger zwitterionic ligand.[44,45]

Electronic Structure

We performed density functional theory (DFT) calculations of the electronic band structures of (SeCYS)PbX_2, including spin−orbit coupling,[46–48] using atomic coordinates obtained from PDF analysis (see Supporting Information for computational details). We address the ligand disorder similarly as in the case of (CYS)$PbCl_2$ by first building an ordered model, assuming a *trans* coordination of SeCYS to the Pb. The calculations indicate a direct bandgap at the Γ point, with E_g values of 0.53 eV and 0.41 eV for X = Cl and Br, respectively (Figures 4A and S10). Although the bandgaps are underestimated, as expected at this level of theory, the difference in gaps between the Cl and Br analogs (0.12 eV) is close to the experimentally measured value (0.21 eV, described later). The valence-band maximum (VBM) consists of 67% (60%) Se and 22% (23%) Pb states, with only 11% (17%) halogen states for (SeCYS)$PbCl_2$ ((SeCYS)$PbBr_2$). The dominant contributions from the chalcogenide at the VBM are also seen in (CYS)PbX_2 (58% S for X = Cl and 52% S for X = Br).[10] The greater contribution of Se states in the VBM of (SeCYS)PbX_2, compared to S states in the VBM of (CYS)PbX_2, is consistent with the lesser electronegativity of Se. The conduction-band minimum (CBM) at the Γ point mostly consists of Pb (>90%) states, with small contributions from halide and chalcogenide states. Therefore, the bandgaps in the organochalcogenide-halide perovskites are mostly determined by the chalcogenide: the higher-energy filled *np* frontier orbitals of Se, compared to those of S, afford a smaller bandgap in (SeCYS)PbX_2. We then compared the band structures of (SeCYS)PbX_2 with those of (CYS)PbX_2 (Figures 4B and S10) arbitrarily aligning the CBM. The band edges remain almost unchanged in shape, with only a higher VBM in (SeCYS)PbX_2, as expected. The calculated carrier effective masses of (SeCYS)PbX_2 are comparable with those in $CsPbX_3$ (e.g., $\langle m^*_h \rangle$ = 0.131, $\langle m^*_e \rangle$ = 0.133 for (SeCYS)$PbBr_2$) as shown in Table S5. Further, we tested the sensitivity of the band structures to the anion arrangements about the central Pb^{2+}. The two structures for the hypothetical $CsPb(SeH)X_2$, where Cs^+ and HSe^- mimic the zwitterionic $^+NH_3(CH_2)_2Se^-$, feature (1) all *trans* and (2) both *cis* and *trans* arrangements of HSe^- in the $[Pb(SeH)_2X_4]^{4-}$ octahedra. The $CsPb(SeH)X_2$ models show similar band dispersion and orbital contributions at the band edges compared with the band structure of (SeCYS)PbX_2, especially at the Γ point (Table S4, Figure S13), indicating that these anion arrangements should have minimal effects on the electronic structure.

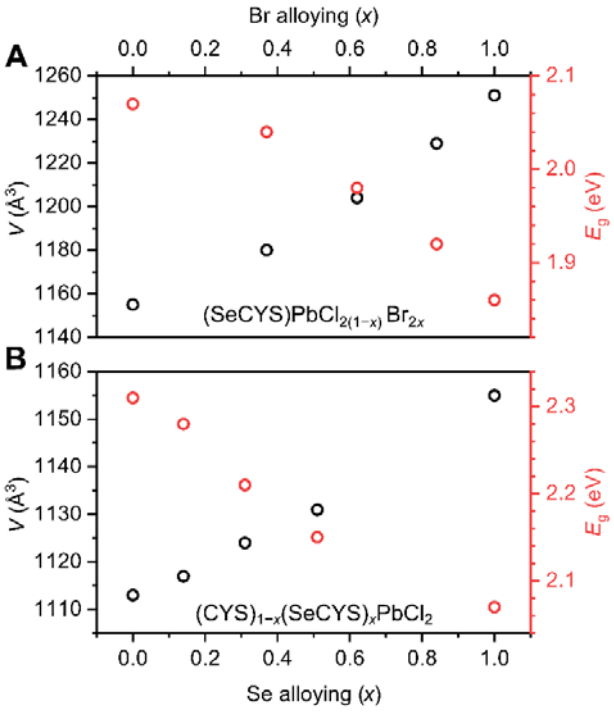

Figure 6. (A) Dependence of the unit-cell volumes (V) and bandgaps (E_g) on the alloying fraction of Br in (SeCYS)$PbCl_{2(1-x)}Br_{2x}$. (B) Dependence of the unit-cell volumes (V) and bandgaps (E_g) on the alloying fraction of SeCYS in $(CYS)_{1-x}(SeCYS)_xPbCl_2$. Unit-cell volumes were extracted by Le Bail refinements. Bandgaps were extracted by Tauc plots.

The valence band dispersion of (SeCYS)PbX_2, and of its model complex $CsPb(SeH)X_2$, is lower than that of a hypothetical $CsPbX_3$ adopting the same lattice constants and space group as for (SeCYS)PbX_2. To test whether the flatter valence band was due to the Se orbitals, we also calculated the band structure of a hypothetical all-Se perovskite: $CsPb(SeH)_3$. We see a sharper dispersion in the valence band of $CsPb(SeH)_3$ compared to the valence band of $CsPbCl_3$ (Figure 5), consistent with the more diffuse Se orbitals providing greater overlap with Pb orbitals. Thus, we conclude that the reduced valence-band dispersion in our calculations of (SeCYS)PbX_2 is due to the anisotropic arrangement of ligands about the central Pb atoms in our models. This conclusion is consistent with the profile of the squared modulus of the electron wave function, corresponding to the VBM (Γ point) shown in Figure S15, which clearly displays an asymmetric orbital environment between the central Pb cation and the adjacent anions, in the case of $CsPb(SeH)X_2$.

The ordered atomistic models used in our DFT calculations cannot capture the distribution of local environments in (SeCYS)PbX_2 and they do not account for structural distortions associated with the inhomogeneous distributions of different Pb environments. However, our calculations hint at the possibility that locally chalcogenide-rich Pb centers (e.g., $Pb(SeCYS)_6$, $Pb(SeCYS)_5X$, etc.), which have a non-zero probability of occurring in the mixed-anion landscape (Figure 3D), may form sub-bandgap trap states.

Alloying the Anion Site

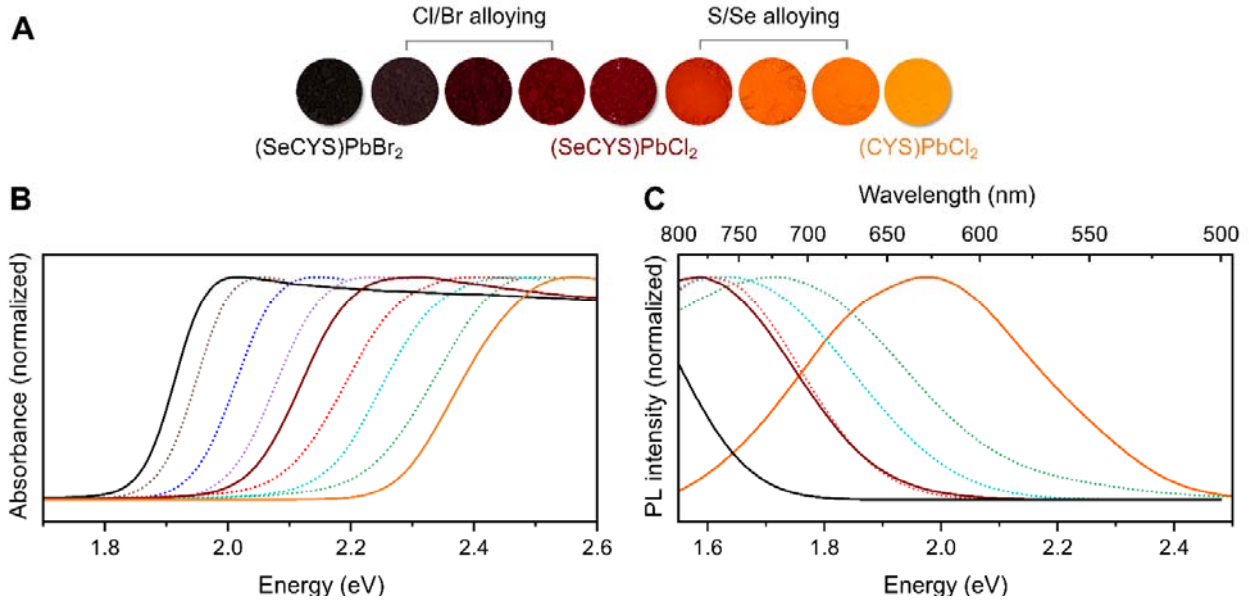

Figure 7. (A) Photographs and (B) diffuse reflectance spectra of powders of (from left to right): (SeCYS)$PbBr_2$ (black line), (SeCYS)$PbCl_{2(1-x)}Br_{2x}$ (solution-state synthesis; dotted lines), (SeCYS)$PbCl_2$ (dark red line), $(CYS)_{1-x}(SeCYS)_xPbCl_2$ (dotted lines), and (CYS)$PbCl_2$ (solid orange line). (C) Photoluminescence (PL) spectra of (SeCYS)$PbBr_2$ (black line), (SeCYS)$PbCl_2$ (dark red line), $(CYS)_{1-x}(SeCYS)_xPbCl_2$ (dotted lines), and (CYS)$PbCl_2$ (solid orange line) measured at 80 K. The full emission of (SeCYS)$PbBr_2$ lies outside the detector range, so the lower-energy emission tail was collected using an IR detector (Figures S22 – S23).

The organochalcogenide-halide perovskites allow us to continuously tune the bandgap by alloying both the chalcogenide and halide sites, since they both contribute states to the VBM, according to the calculated electronic structures.

Halide alloying for (SeCYS)$PbCl_{2(1-x)}Br_{2x}$ was conducted by tuning bromide and chloride concentrations in the precursor solution (solution-state synthesis). We found that ball-milling together different ratios of the solid perovskite endmembers: (SeCYS)$PbCl_2$ and (SeCYS)$PbBr_2$ (mechanochemical synthesis), could also form (SeCYS)$PbCl_{2(1-x)}Br_{2x}$, similar to the mechanochemical syntheses of mixed-halide[8,40] and mosaic[49] perovskites. Chalcogenide alloying for $(CYS)_{1-x}(SeCYS)_xPbX_2$ (X = Cl, Br) was accomplished by tuning the ratio of the two ligands in the solution-state synthesis (see Supporting Information for detailed synthetic procedures). Notably, we were unable to mix the chalcogenides through a mechanochemical synthesis, starting directly from the two endmembers: (CYS)$PbCl_2$ and (SeCYS)$PbCl_2$ (Figures S20, S21). Our ability to mechanochemically alloy the halide but not the chalcogenide corroborates the lower mobility of the larger zwitterionic ligand and its stronger bond with Pb compared to those with the halides, which are also supported by the 2D ^{207}Pb NMR studies.

The alloyed perovskites were characterized by PXRD and Le Bail refinements to obtain unit-cell parameters (Figures S24 – S29, Table S6). The compositions of the alloyed perovskites were determined by ^{1}H NMR (of the dissolved product) to quantify the ratios of SeCYS and CYS ligands, and inductively coupled plasma mass spectrometry (ICP-MS) to quantify the Pb to Br ratios (Figures S18, S19). The dependence of unit-cell volumes on the anion alloying ratio is summarized in Figure 6. Combining both the Cl/Br and S/Se alloying strategies, we realized three series of compositions: i) (SeCYS)$PbCl_{2(1-x)}Br_{2x}$ (through solution- and solid-state syntheses), ii) $(CYS)_{1-x}(SeCYS)_xPbCl_2$, and iii) $(CYS)_{1-x}(SeCYS)_xPbBr_2$.

Optical Properties

We obtained optical gaps of 2.07 eV and 1.86 eV for (SeCYS)$PbCl_2$ and (SeCYS)$PbBr_2$, respectively, using diffuse reflectance spectroscopy and direct-bandgap Tauc plots (Figures 7A and S9). In accordance with the calculated band structures, the bandgaps of the organochalcogenide-halide perovskites exhibit a redshift from S to Se and from Cl to Br leading to the bandgap ordering: (CYS)$PbCl_2$ > (CYS)$PbBr_2$ > (SeCYS)$PbCl_2$ > (SeCYS)$PbBr_2$. Combining both the Cl/Br and S/Se alloys allows us to continuously tune the bandgap from 2.07 to 1.86 eV for the (SeCYS)$PbCl_{2(1-x)}Br_{2x}$ series (Figures 6, 7B), from 2.31 to 2.07 eV for the $(CYS)_{1-x}(SeCYS)_xPbCl_2$ series, (Figures 6, 7B) and from 2.16 to 1.86 eV for the $(CYS)_{1-x}(SeCYS)_xPbBr_2$ series (Figure S21).

Similar to (CYS)PbX_2, (SeCYS)PbX_2 and its alloys show no room-temperature photoluminescence (PL) and a broad, Stokes shifted PL at 80 K. The 80-K emission maxima of 1.58 eV and ca. 1.4 eV, for (SeCYS)PbX_2 with X = Cl and Br, respectively, (Figure 7C) are considerably redshifted compared to those of the (CYS)PbX_2 analogs (1.98 and 1.66 eV for X = Cl and Br, respectively).[10] Because much of the emission from (SeCYS)$PbBr_2$ falls outside the detector range, we used an IR detector to estimate the PL maximum (Figures S22 – S23). The broad emission with a large (ca. 0.5 eV) Stokes shift is potentially indicative of trap states originating from selenide-rich local coordination or from other defects.

Powders of (SeCYS)$PbCl_2$ and (SeCYS)$PbBr_2$, exposed to 1-sun illumination in air at 40 °C, maintain their PXRD patterns over the course of 4 days, with some reduction of crystallinity

evident after 27 days although we do not see the growth of new crystalline phases (Figure S30). The longer-term stability of the organochalcogenide-halide perovskites should be further assessed.

Conclusion

We present the first examples of organoselenide-halide perovskites: (SeCYS)PbX_2 (X = Cl, Br). The zwitterionic organoselenide ligand occupies both the A^+ site and X^- site in the prototypical ABX_3 perovskite, further expanding the family of organochalcogenide-halide perovskites, in addition to the recently reported organosulfide-halide perovskites: (CYS)PbX_2.[10] X-ray diffraction and total scattering reveal disordered anions over long length scales in the average structures, and a systematic lattice expansion with (CYS)$PbCl_2$ < (SeCYS)$PbCl_2$ < (CYS)$PbBr_2$ < (SeCYS)$PbBr_2$. The ligand dynamics and rotational isomerism were probed by Raman spectroscopy. Further, we apply solid-state ^{77}Se and ^{207}Pb NMR to study the local structures of the organochalcogenide-halide perovskites, complemented by theoretical simulations of the distributions of different coordination environments. We find that the heteroanionic perovskites LPbX_2 (L = CYS, SeCYS) can be viewed as solid solutions with the chalcogenide/halide randomly distributed at the anion site, similar, but not identical, to mixed-halide perovskites with a 2:1 ratio between different halides.

The incorporation of Se affords smaller bandgaps compared to the S analogs, with gaps of 2.07 eV and 1.86 eV for (SeCYS)$PbCl_2$ and (SeCYS)$PbBr_2$, respectively. The electronic effects of Se substitution were further studied by DFT, revealing reduced bandgaps, which we attribute to the higher frontier p orbital energy level in Se compared to that of S. Using both solution-state and solid-state mechanochemical syntheses, we demonstrate halide alloying and chalcogenide alloying to afford a continuous bandgap shift from 1.86 to 2.31 eV with the bandgap increasing as (SeCYS)$PbBr_2$ < (SeCYS)$PbCl_{2(1-x)}Br_{2x}$ < (SeCYS)$PbCl_2$ < $(CYS)_{1-x}(SeCYS)_xPbCl_2$ < (CYS)$PbCl_2$. These bandgaps, encompassing near-ideal values for the top absorber in tandem solar cells,[11] or for photocatalysis with visible light,[50] motivate further studies to form films of organochalcogenide-halide perovskites and tune their defect chemistry to assess their potential for photocarrier extraction.

Knowledge of both the long-range structure and distribution of local structures, presented here, will be important to understand and exploit the, as yet unoptimized, optoelectronic properties of this nascent family of organochalcogenide-halide perovskites. Further studies should probe whether the local disorder seen in the solid-state NMR studies (Figure 3) leads to chalcogen-rich sub-bandgap trap states, as suggested by the lower bandgaps computed through DFT of chalcogen-rich models (Figure 5), and how these potential trap states, or other photoluminescence-quenching defects (e.g., halogen vacancies), can be suppressed. Furthermore, the organochalcogenides exhibit much lower anion mobility than the halides, based on 2D NMR and mechanochemical synthetic attempts, likely due to the ligand size and stronger bonding enthalpy with Pb. The immobility of anions, at least in part of the inorganic framework, may enhance stability, potentially mitigating the well-known halide mobility[44,51,52] and light-induced halide segregation in mixed-halide perovskites.[8] Overall, the introduction and expansion of the family of organochalcogenide-halide perovskites offer new handles for tuning the properties of halide perovskites using insights from solid-state as well as organo-main-group chemistry.

Acknowledgements

This work was funded by the Brown Science Foundation and the mechanochemical syntheses and characterization were supported by the NSF Center for the Mechanical Control of Chemistry, CHE-2303044. J.L. acknowledges a Stanford Interdisciplinary Graduate Fellowship. We thank Siyu (Richard) Chen for algorithm coding, Jamie Cleron for ICP-MS analysis, Dr. S. R. Lynch for ^{1}H NMR analysis, and Prof. V. K. Michaelis at the University of Alberta for discussion on the ^{207}Pb NMR analysis. J.A.R. and Y.W. acknowledge support from AccelNet Collaborative Research for Sustainable Capture and Conversion of CO_2 to Chemicals and Fuels using Renewable Electrons (SCO_2RE) funded by the National Science Foundation (NSF, 1927325) for NMR studies. We thank Drs. Hasan Celik, Raynald Giovine, and UC Berkeley's NMR facility in the College of Chemistry (CoC-NMR) for NMR spectroscopic assistance. M.R.F. acknowledges support of the John Fell Oxford University Press (OUP) Research Fund for computational work. S.S. and M.R.F. acknowledge support from the UK Engineering and Physical Sciences Research Council (EPSRC), Grant EP/V010840/1. S.S. and M.R.F. accessed computational resources via our membership of the UK's HEC Materials Chemistry Consortium, which is funded by EPSRC (EP/R029431). SC-XRD studies were performed at the Stanford Nano Shared Facilities (SNSF), supported by the NSF under the award ECCS-1542152. This research used resources of the Advanced Photon Source, a U.S. Department of Energy (DOE) Office of Science User Facility operated for the DOE Office of Science by Argonne National Laboratory under Contract No. DE-AC02-06CH11357. The mail-in program at Beamline 11-ID-B contributed to the data.

Keywords: organochalcogenide • halide perovskites • solid-state NMR • band structure

[1] J. D. Donaldson, D. Laughlin, S. D. Ross, J. Silver, *J. Chem. Soc., Dalton Trans.* **1973**, 1985–1988.
[2] R. Matheu, J. A. Vigil, E. J. Crace, H. I. Karunadasa, *Trends Chem.* **2022**, *4*, 206–219.
[3] A. Kojima, K. Teshima, Y. Shirai, T. Miyasaka, *J. Am. Chem. Soc.* **2009**, *131*, 6050–6051.
[4] M. A. Green, A. Ho-Baillie, H. J. Snaith, *Nature Photon* **2014**, *8*, 506–514.
[5] J. Seo, J. H. Noh, S. I. Seok, *Acc. Chem. Res.* **2016**, *49*, 562–572.
[6] M. S. G. Hamed, G. T. Mola, *Critical Reviews in Solid State and Materials Sciences* **2020**, *45*, 85–112.
[7] B. Chen, X. Zheng, Y. Bai, N. P. Padture, J. Huang, *Advanced Energy Materials* **2017**, *7*, 1602400.
[8] E. T. Hoke, D. J. Slotcavage, E. R. Dohner, A. R. Bowring, H. I. Karunadasa, M. D. McGehee, *Chem. Sci.* **2014**, *6*, 613–617.

[9] M. C. Brennan, A. Ruth, P. V. Kamat, M. Kuno, *Trends in Chemistry* **2020**, *2*, 282–301.
[10] J. Li, Z. Chen, S. Saha, J. K. Utterback, M. L. Aubrey, R. Yuan, H. L. Weaver, N. S. Ginsberg, K. W. Chapman, M. R. Filip, H. I. Karunadasa, *J. Am. Chem. Soc.* **2022**, *144*, 22403–22408.
[11] R. W. Crisp, G. F. Pach, J. M. Kurley, R. M. France, M. O. Reese, S. U. Nanayakkara, B. A. MacLeod, D. V. Talapin, M. C. Beard, J. M. Luther, *Nano Lett.* **2017**, *17*, 1020–1027.
[12] T. Umebayashi, K. Asai, T. Kondo, A. Nakao, *Phys. Rev. B* **2003**, *67*, 155405.
[13] S. Suresh, A. R. Uhl, *Advanced Energy Materials* **2021**, *11*, 2003743.
[14] T. K. Todorov, J. Tang, S. Bag, O. Gunawan, T. Gokmen, Y. Zhu, D. B. Mitzi, *Advanced Energy Materials* **2013**, *3*, 34–38.
[15] M. L. Agiorgousis, Y.-Y. Sun, D.-H. Choe, D. West, S. Zhang, *Advanced Theory and Simulations* **2019**, *2*, 1800173.
[16] M.-G. Ju, J. Dai, L. Ma, X. C. Zeng, *Adv. Energy Mater.* **2017**, *7*, 1700216.
[17] Y.-Y. Sun, M. L. Agiorgousis, P. Zhang, S. Zhang, *Nano Lett.* **2015**, *15*, 581–585.
[18] H. Zhang, X. Wu, K. Ding, L. Xie, K. Yang, C. Ming, S. Bai, H. Zeng, S. Zhang, Y.-Y. Sun, *Chem. Mater.* **2023**, DOI 10.1021/acs.chemmater.2c03676.
[19] Z. Li, K.-H. Xue, J. Wang, J.-G. Li, X. Ao, H. Sun, X. Song, W. Lei, Y. Cao, C. Wang, *ACS Appl. Mater. Interfaces* **2020**, *12*, 41259–41268.
[20] S. A. Siddiqi, A. Aslam, S. Naseem, *Mod. Phys. Lett. B* **2001**, *15*, 973–980.
[21] Deposition Number 2270130 (for (SeCYS)$PbCl_2$) Contains the Supplementary Crystallographic Data for This Paper. These Data Are Provided Free of Charge by the Joint Cambridge Crystallographic Data Centre and Fachinformationszentrum Karlsruhe Access Structures Service., **n.d.**
[22] C. R. Morelock, B. K. Greve, M. Cetinkol, K. W. Chapman, P. J. Chupas, A. P. Wilkinson, *Chem. Mater.* **2013**, *25*, 1900–1904.
[23] R. D. Shannon, *Acta Cryst. A* **1976**, *32*, 751–767.
[24] O. Yaffe, Y. Guo, L. Z. Tan, D. A. Egger, T. Hull, C. C. Stoumpos, F. Zheng, T. F. Heinz, L. Kronik, M. G. Kanatzidis, J. S. Owen, A. M. Rappe, M. A. Pimenta, L. E. Brus, *Phys. Rev. Lett.* **2017**, *118*, 136001.
[25] K. Nakada, Y. Matsumoto, Y. Shimoi, K. Yamada, Y. Furukawa, *Molecules* **2019**, *24*, 626.
[26] S. Bloxham, O. Eicher-Lorka, R. Jakubėnas, G. Niaura, *Spectroscopy Letters* **2003**, *36*, 211–226.
[27] L. Riauba, G. Niaura, O. Eicher-Lorka, E. Butkus, *J. Phys. Chem. A* **2006**, *110*, 13394–13404.
[28] L. S. Wong, V. L. Vilker, W. T. Yap, V. Reipa, *Langmuir* **1995**, *11*, 4818–4822.
[29] D. Lin-Vien, N. B. Colthup, W. G. Fateley, J. G. Grasselli, in *The Handbook of Infrared and Raman Characteristic Frequencies of Organic Molecules*, Elsevier, **1991**, pp. 225–250.
[30] J. R. Durig, H. V. Phan, M. M. Bergana, M. S. Rollins, J. M. Gulick, J. D. Odom, S. D. Hudson, *Spectrochimica Acta Part A: Molecular Spectroscopy* **1994**, *50*, 399–419.
[31] A. Kudelski, W. Hill, *Langmuir* **1999**, *15*, 3162–3168.
[32] D. Stefańska, M. Ptak, M. Mączka, *Molecules* **2022**, *27*, 7949.
[33] J. K. Harada, N. Charles, K. R. Poeppelmeier, J. M. Rondinelli, *Adv. Mater.* **2019**, *31*, 1805295.
[34] H. Kageyama, K. Hayashi, K. Maeda, J. P. Attfield, Z. Hiroi, J. M. Rondinelli, K. R. Poeppelmeier, *Nat. Commun.* **2018**, *9*, 772.
[35] H. Duddeck, in *Annual Reports on NMR Spectroscopy*, Academic Press, **2004**, pp. 105–166.
[36] N. P. Luthra, J. D. Odom, in *Organic Selenium and Tellurium Compounds (1986)*, John Wiley & Sons, Ltd, **1986**, pp. 189–241.
[37] D. J. Kubicki, S. D. Stranks, C. P. Grey, L. Emsley, *Nat. Rev. Chem.* **2021**, *5*, 624–645.
[38] L. Piveteau, V. Morad, M. V. Kovalenko, *J. Am. Chem. Soc.* **2020**, *142*, 19413–19437.
[39] B. Wrackmeyer, *Application of 207Pb NMR Parameters*, Elsevier Science & Technology Books, **2002**.
[40] A. Karmakar, A. M. Askar, G. M. Bernard, V. V. Terskikh, M. Ha, S. Patel, K. Shankar, V. K. Michaelis, *Chem. Mater.* **2018**, *30*, 2309–2321.
[41] A. M. Askar, A. Karmakar, G. M. Bernard, M. Ha, V. V. Terskikh, B. D. Wiltshire, S. Patel, J. Fleet, K. Shankar, V. K. Michaelis, *J. Phys. Chem. Lett.* **2018**, *9*, 2671–2677.
[42] A. Karmakar, M. S. Dodd, X. Zhang, M. S. Oakley, M. Klobukowski, V. K. Michaelis, *Chem. Commun.* **2019**, *55*, 5079–5082.
[43] D. Massiot, I. Farnan, N. Gautier, D. Trumeau, A. Trokiner, J. P. Coutures, *Solid State Nuclear Magnetic Resonance* **1995**, *4*, 241–248.
[44] A. Senocrate, I. Moudrakovski, G. Y. Kim, T.-Y. Yang, G. Gregori, M. Grätzel, J. Maier, *Angew. Chem. Int. Ed.* **2017**, *56*, 7755–7759.
[45] A. M. A. Leguy, J. M. Frost, A. P. McMahon, V. G. Sakai, W. Kockelmann, C. Law, X. Li, F. Foglia, A. Walsh, B. C. O'Regan, J. Nelson, J. T. Cabral, P. R. F. Barnes, *Nat. Commun.* **2015**, *6*, 7124.
[46] P. Hohenberg, W. Kohn, *Phys. Rev.* **1964**, *136*, B864–B871.
[47] J. P. Perdew, K. Burke, M. Ernzerhof, *Phys. Rev. Lett.* **1996**, *77*, 3865–3868.
[48] M. I. Aroyo, D. Orobengoa, G. de la Flor, E. S. Tasci, J. M. Perez-Mato, H. Wondratschek, *Acta Cryst. A* **2014**, *70*, 126–137.
[49] J. Li, R. Matheu, F. Ke, Z. Liu, Y. Lin, H. I. Karunadasa, *Angewandte Chemie International Edition* **2023**, *62*, e202300957.
[50] S. Park, W. J. Chang, C. W. Lee, S. Park, H.-Y. Ahn, K. T. Nam, *Nat Energy* **2016**, *2*, 1–8.
[51] A. Walsh, S. D. Stranks, *ACS Energy Lett.* **2018**, *3*, 1983–1990.
[52] J. Mizusaki, K. Arai, K. Fueki, *Solid State Ionics* **1983**, *11*, 203–211.